

MoS₂ and Janus (MoSSe) Based 2D van der Waals Heterostructures: Emerging Direct Z-scheme Photocatalysts[†]

Arunima Singh*, Manjari Jain, Saswata Bhattacharya*

Department of Physics, Indian Institute of Technology Delhi, Hauz Khas, New Delhi:110016, India

E-mail: saswata@physics.iitd.ac.in[SB], Arunima.Singh@physics.iitd.ac.in[AS]

Phone: +91-2659 1359. Fax: +91-2658 2037

Abstract

Two-dimensional (2D) materials viz. transition metal dichalcogenides (TMD) and transition metal oxides (TMO) offer a platform that allows creation of heterostructures with a variety of properties. The optoelectronic industry has observed an upheaval in the research arena of MoS₂ based van der Waals (vdW) heterostructures (HTSs) and Janus structures. Therefore, interest towards these structures are backed by the selectivity in terms of electronic and optical properties. The present study investigates the photocatalytic ability of bilayer, MoS₂ and Janus (MoSSe) based vdW HTSs viz. MoS₂/TMO, MoS₂/TMD, MoSSe/TMO and MoSSe/TMD, by first-principles based approach under the framework of (hybrid) density functional theory (DFT) and many body perturbation theory (GW approximation). We have considered HfS₂, ZrS₂, TiS₂, WS₂ and HfO₂, T-SnO₂, T-PtO₂ from the family of TMD and TMO, respectively. The photocatalytic properties of these vdW HTSs are thoroughly investigated and compared with the respective individual monolayers by visualizing their band edge alignment,

electron-hole recombination and optical properties. Strikingly we observe that, despite most of the individual monolayers do not perform optimally as a photocatalyst, type II band edge alignment is noticed to vdW HTSs and they appear to be efficient for photocatalysis via Z-scheme. Moreover, these HTSs have also shown promising optical response in the visible region. Finally electron-hole recombination, H₂O adsorption and hydrogen Evolution Reaction (HER) results establish that MoSSe/HfS₂, MoSSe/TiS₂, MoS₂/T-SnO₂, MoS₂/ZrS₂ and MoSSe/ZrS₂ are probable, most efficient Z-scheme photocatalysts.

Introduction

In present context, solar energy is the supreme resource to combat energy and environment related issues. With an aim to enhance the utilization of solar energy, the field of photocatalysis for water splitting and pollutant degradation have gained interest.¹⁻⁴ Further, the demand for exciting materials that serve selectivity, have directed the focus towards the 2D materials. Amongst these, MoS₂ is one of the widely studied 2D materials that belongs to the transition metal dichalcogenides (TMD) family. The other classification constitutes graphene family, transition metal oxides (TMOs) and MXenes.⁵ These materials have been vastly studied in the regimes of defect study,^{6,7} photovoltaics^{8,9} and optoelectronics.^{10,11} These widely studied (both theoretically and experimentally) TMDs are MoS₂, MoSe₂, WS₂ and WSe₂. However, other TMDs such as HfS₂, ZrS₂ and TiS₂ have also been a matter of research for their salient electronic, vibrational and optical properties.¹²⁻¹⁴ Conversely, TMOs have not been established with similar level of experimental database as of TMDs. Lebègue *et al.*¹⁵ indicate synthesis of TMOs as challenging due to the rare occurrence of their stable bulk phases. Only few of these materials have been synthesized experimentally.¹⁶ In this scenario, theoretical studies of the TMOs have showcased a huge potential, which helps in opening the scope of further research.^{17,18} Another class of 2D materials that have recently drawn a lot of interest is Janus.^{19,20} These materials, having the form of MXY (M = Mo and

and (b) Z-scheme systems. In former, Conduction Band Minimum (CBm) and Valence Band Maximum (VBM) of the vdW HTSs, straddle the redox potential.^{42,43} Here CBm and VBM are on two different monolayers thereby facilitating spatial charge separation with reduction and oxidation reactions on different monolayer, respectively. But, to achieve sufficient redox ability for a specific reaction occurring on a single photocatalyst, a larger bandgap, that simultaneously inhibit $e^- - h^+$ recombination and correlates to higher oxidation/reduction ability, is required. However, to enhance the efficiency, a smaller bandgap is desirable to increase the efficiency of light harvesting. Therefore, it is of a paramount importance for improving the photocatalytic performance, where Z-scheme⁴⁴⁻⁴⁶ brings the solution by manipulating the photogenerated $e^- - h^+$ pairs as shown in the Z-scheme mode (see Fig. 1). Like before, here as well having type II alignment is mandatory but the CBm and VBM of the vdW HTSs do not straddle the redox potentials in the same manner as before. The layer with CBm straddling the reduction level and the another layer with VBM straddling the oxidation level are involved in hydrogen evolution reaction (HER) and oxygen evolution reaction (OER), respectively (see Fig. 1). The higher interlayer recombination of $e^- - h^+$ as compared to that of intralayer is a necessary step in the process. Thus, photoabsorption is improved due to two different band gaps leading to HER and OER on different systems.⁴⁷⁻⁴⁹ The weak vdW interlayer interaction in vdW HTSs facilitates lubricancy or interlayer movement that further assists the Z-scheme photocatalysis.⁴¹ Although, some vdW HTSs have been studied under this regime,^{41,44,50,51} no extensive study on MoS₂ based vdW HTSs consisting of TMDs (viz. HfS₂, ZrS₂, TiS₂) and TMOs (viz. HfO₂, T-PtO₂, T-SnO₂) as second layer are observed so far. On a similar note, the database of Janus (MoSSe) based vdW HTSs for the photocatalytic application is at an initial stage.^{20,24} Hence, there is a justified interest to explore their applicability as photocatalysts. The MoSSe based vdW HTSs have further given rise to two possible stacking arrangements. Contrary to the structure of MoS₂, the MoSSe lacks mirror symmetry. Hence, it is crucial to compare the possible stacking configurations of MoSSe based vdW HTSs with the MoS₂ based vdW HTSs, for the photo-

catalytic application.

In this article, we have presented an exhaustive comparative study of MoS₂ and MoSSe based vdW HTSs, where the second layer is from the family of (i) TMDs viz. WS₂, HfS₂, ZrS₂, TiS₂ and (ii) TMOs viz. HfO₂, T-PtO₂, T-SnO₂. The existing literatures so far, have not discussed the above listed vdW HTS configurations for the Z-scheme photocatalysis. Until date earlier reports exist only on monolayers of type II vdW HTSs of TMDs and TMOs for photocatalytic applications.⁵² Here, using state-of-the-art theoretical methodologies within the framework of hybrid density functional theory (DFT) and manybody perturbation theory (MBPT) (viz. G₀W₀) we have systematically studied the important parameters for photocatalytic applications. First, we introduce the different possible stable configurations of vdW HTSs. Next we discuss the band edge alignment of 2D monolayers and their corresponding vdW HTSs. Subsequently, their recombination path is well analyzed to check capability as a Z-scheme photocatalyst. Finally, their accurate optical response is computed and understood with MBPT technique for consideration in photocatalytic devices. Strikingly we observe that, despite most of the individual monolayers do not perform optimally as a photocatalyst, type II band edge alignment is noticed to vdW HTSs and they appear to be efficient for photocatalysis via Z-scheme.

Methodology

We have employed first-principles based methodology under the framework of DFT.⁵³⁻⁵⁸ The PAW pseudopotentials are used in our calculations using plane wave basis set as employed in Vienna *Ab initio* Simulation Package (VASP).⁵⁹⁻⁶¹ The exchange-correlation (xc) interaction amongst electrons are accounted by Generalized Gradient Approximation (GGA) with the functional form as proposed by Perdew-Burke-Ernzerhof (PBE).^{62,63} The hybrid density functional has also been employed to account for the same with the functional proposed by

Heyd-Scuseria-Ernzerhof (HSE06).⁶⁴ The hybrid functional (HSE06) considers 25% mixing (α) of the short range Hartree-Fock (HF) exchange. Its long range part is described by GGA-PBE functional.

The vdW HTSs are optimized using PBE functional and HSE06 is used to determine single point energy. The conjugate gradient minimization is performed with the Brillouin Zone (BZ) sampling of $2 \times 2 \times 1$ K-grid and the energetics are obtained by the BZ sampling of $16 \times 16 \times 1$ K-grid. The energy tolerance of 0.001 meV and force tolerance of 0.001 eV/Å have been used for optimization. In the ground state calculations, the plane wave cut-off energy is set to 600 eV. The vdW HTSs are modelled with 20 Å vacuum in order to avoid electrostatic interactions between the periodic images. The two-body vdW interaction as devised by Tkatchenko-Scheffler has been employed.^{65,66} The correction parameter is based on Hirshfeld partitioning of the electron density. Note that, we have not included spin-orbit coupling (SOC) in our calculations, since the previous literatures have reported only slight change in band gap due to the same.^{44,67,68} The optical properties are calculated using the GW approach.^{69,70} We have performed hybrid calculations (HSE06), as an initial step for single shot GW calculations [i.e. $G_0W_0@HSE06$].

Results and Discussions

Heterostructure stacking

We have constructed commensurate bilayer vdW HTSs⁷¹ with minimum lattice mismatch between the layers. The vdW HTSs have been formed with monolayer of MoS₂ (or MoSSe) along with that of WS₂, ZrS₂, HfS₂, TiS₂, HfO₂, T-PtO₂ and T-SnO₂, in vertical alignment. The specifications of the monolayers (see lattice parameters in SI) corroborate with the existing literature.^{52,72,73} All the monolayers are constituted as $2 \times 2 \times 1$ supercell (24 atoms) except ZrS₂ and HfS₂, where $\sqrt{3} \times \sqrt{3} \times 1$ supercell consists of 21 atoms. Here, the stacking styles between two monolayers have not been varied in each vdW HTS. This is due to the fact

that, the binding energy change of merely few meV is observed with the change in stacking styles of two monolayers in a particular vdW HTS.^{74,75}

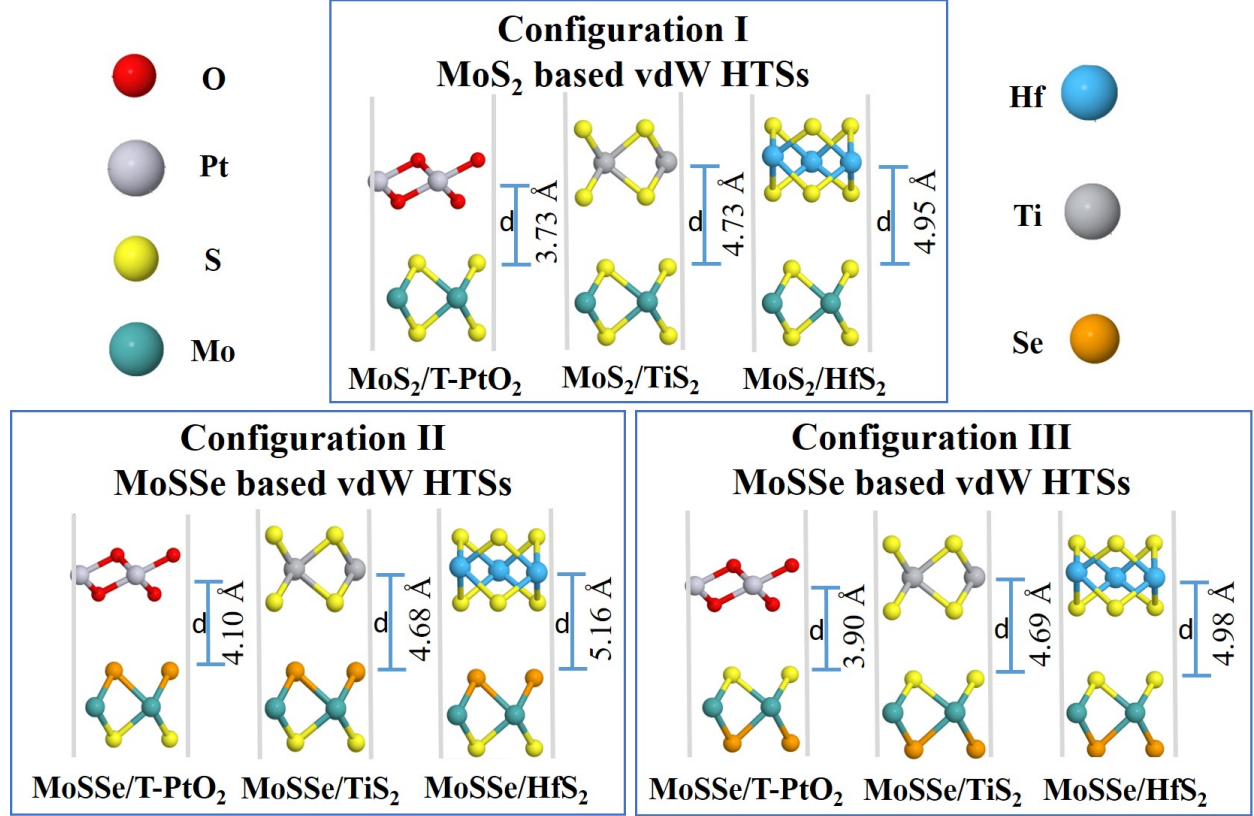


Figure 2: (Color online) vdW HTSs with configuration I, II and III. MoS₂/BX₂ (configuration I), MoSSe/BX₂ (configuration II), where Se atomic layer is at interface and MoSSe/BX₂ (configuration III), where S atomic layer is at interface.

We have calculated the binding energy of vdW HTSs by the expression,⁷⁴

$$E_b = E(\text{vdW HTSs}) - E(\text{MoS}_2 \text{ or MoSSe}) - E(\text{BX}_2) \quad (1)$$

where E_b is the binding energy of the vdW HTS MoS₂/BX₂ (or MoSSe/BX₂); $E(\text{MoS}_2)$ is the energy of monolayer MoS₂; $E(\text{MoSSe})$ is the energy of monolayer MoSSe and $E(\text{BX}_2)$ is the energy of monolayer BX₂ (where B = W, Hf, Zr, Pt, Sn and X = S or O).

Fig. 2 shows the three configuration of vdW HTSs as considered in the present work. Configuration I is of the type MoS₂/BX₂. The stacking type of MoS₂/T-SnO₂, MoS₂/ZrS₂

Table 1: The corresponding bilayer vdW HTS lattice mismatch and binding energies of different configurations (MoS₂/BX₂(I), MoSSe/BX₂(II and III)) are enlisted

BX ₂	Lattice mismatch (%)	Binding Energy (eV)		
		I	II	III
WS ₂	0.0	-1.04	-1.05	-1.02
ZrS ₂	2.5	-0.49	-0.54	-0.52
HfS ₂	3.9	-0.30	-0.35	-0.33
TiS ₂	2.5	-0.45	-1.00	-0.94
HfO ₂	1.2	-0.40	-0.54	-0.47
T-PtO ₂	0.4	-0.83	-0.63	-0.68
T-SnO ₂	1.8	-2.19	-2.24	-2.22

and MoS₂/WS₂(or HfO₂) are same as that of MoS₂/T-PtO₂, MoS₂/HfS₂ and MoS₂/TiS₂, respectively. On replacing MoS₂ with MoSSe, we have constituted configuration II and III. The former consists of Se atomic layer of MoSSe at the interface, whereas the latter has S atomic layer at the interface. Configuration II and III also follow the same analogy as configuration I. Table 1 enlists the lattice mismatch and the binding energy of all the vdW HTS configurations. We define the mismatch as $(l(\text{MoS}_2) - l(\text{BX}_2))/l(\text{BX}_2)$, where l is the lattice constant of MoS₂ and BX₂ respectively.

Band edge alignment

The photocatalytic applications require the understanding of band gaps and absolute band edge positions. We have calculated these with both PBE and HSE06 functionals. Fig. 3(a) provides band edge alignment of the monolayers. We observe here that the chosen monolayers for vdW HTSs have type II heterojunction. In the Fig. 3, H⁺/H₂ and O₂/H₂O correspond to the reduction and oxidation potential of water splitting, respectively, both for pH(0) (solid line) and pH(7) (dashed line). Fig. 3(a) shows that HSE06 and PBE have sufficient discrepancies in estimating band edge positions. Calculations with HSE06 functional incorporate HF exact exchange term resulting due to self-interaction error of e⁻, which is not well taken care of in the case of PBE functional. Hence, the results presented in further plots are carried

out by the HSE06 functional.

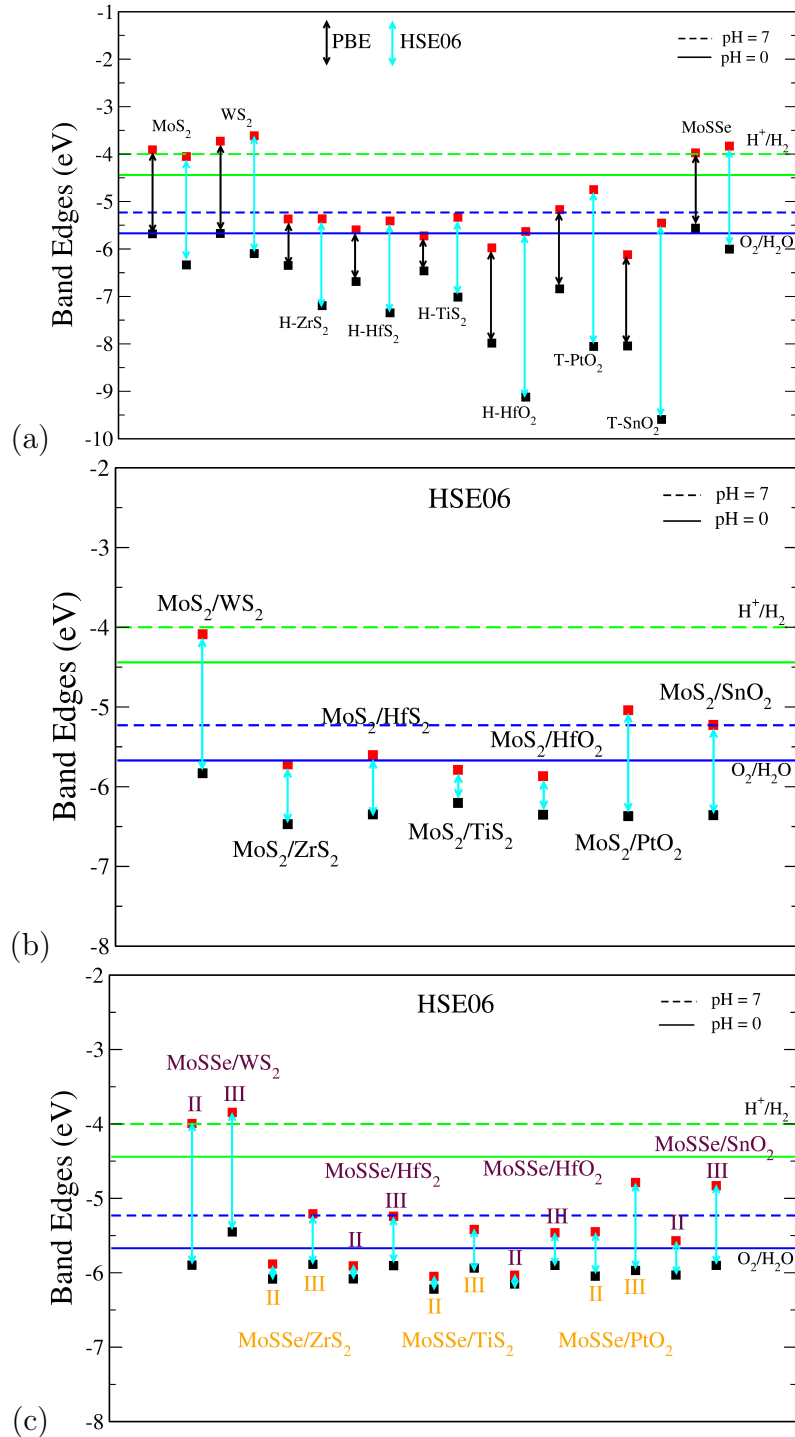


Figure 3: (Color online) Band edge alignment with respect to water redox potentials of (a) individual monolayers, (b) MoS_2/BX_2 vdW HTSs (configuration I), (c) $MoSSe/BX_2$ vdW HTSs (configuration II and III), where BX_2 refers to WS_2 , ZrS_2 , HfS_2 , TiS_2 , HfO_2 , PtO_2 and SnO_2 .

Fig. 3(b) and Fig. 3(c) depict the absolute band edge positions of the MoS₂ and MoSSe based vdW HTSs, respectively. Fig. 3(b) indicates that individual band alignment approximately predicts the combined alignment of the vdW HTSs. The weak vdW interaction between 2D monolayers is attributed to the aforementioned indication. Here, the type II alignment can be seen with VBM of MoS₂ (or MoSSe) monolayer and CBm of HfS₂, ZrS₂, TiS₂, HfO₂, T-PtO₂ and T-SnO₂ monolayers. The band gaps of the monolayers and vdW HTSs are listed in SI (Table I). Now, the CBm and VBM should lie a few eVs above and below the redox potentials for the material to be good for photocatalysis. However, in our case the vdW HTS band gap does not straddle the photocatalytic water splitting potentials. Hence, we analyze these bilayer vdW HTSs for their applicability as Z-scheme photocatalyst. The vdW HTSs deduced for further analysis from Fig. 3 are the configurations consisting HfS₂, ZrS₂, TiS₂, HfO₂, T-PtO₂ and T-SnO₂. Note that MoS₂ (or MoSSe) monolayer (CBm) does form type II alignment with WS₂ (VBM) as well and the HTS is observed to be capable for photocatalysis (but not via Z-scheme). However, we have included this in our manuscript as a reference, with an intention to showcase clear distinction w.r.t Z-scheme photocatalysts. Moreover, on observing Fig. 3(c) a unanimously similar trend infers that the band gap of vdW HTSs of configuration II is significantly different than that of configuration III.

It should be noted that the absolute band edge alignment is obtained with respect to the zero vacuum level. The associated E_{vac} (vacuum level) of each calculation is obtained from the electrostatic potential of the system. As is evident from the term, the plot explains the electrostatic potential corresponding to each atomic layer (see Fig. 4). It is pertinent to understand the plot as it informs about the work function and potential difference between the monolayers. Thus, we are able to analyze the interlayer charge transfer that indicates the photocatalytic strength. Fig. 4 corresponds to the electrostatic potential plot of MoS₂/WS₂. Considering left to right chronology in Fig. 4(a), we observe the potential of S, Mo, S atomic layers of MoS₂ monolayer and S, W, S atomic layers of WS₂ monolayer. We see a clear difference in the potentials of cationic layers viz. Mo and W atomic layers. The gradient

between the monolayers facilitate the charge separation between them. Fig. 4(b) shows the corresponding MoS₂/WS₂ vdW HTS describing the respective atomic layers.

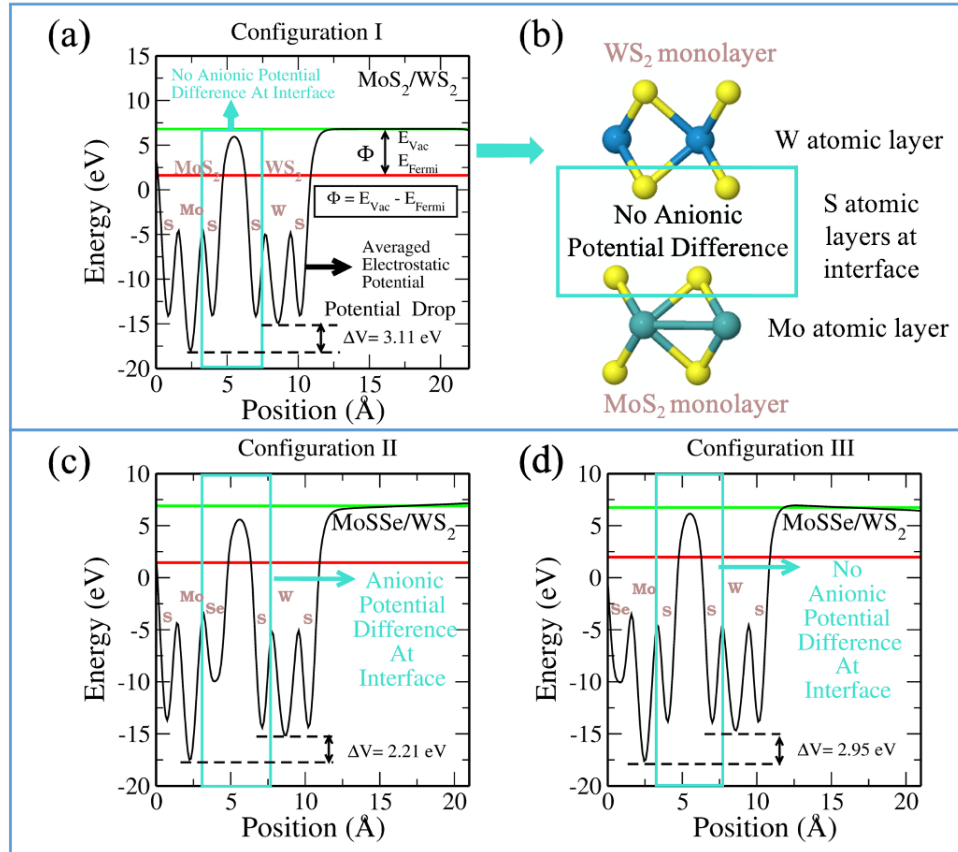


Figure 4: (Color online) Electrostatic potential plot of MoS₂/WS₂ depicting (a) the potential difference, (b) the work function in configuration I, (c) cationic and anionic potential difference in configuration II, and (d) configuration III.

Fig. 4(c) and (d), show the plots for MoSSe/WS₂ configuration II and III, respectively. We observe, that in configuration II (Fig. 4(c)) there is an additional potential gradient between Se atomic layer of MoSSe and S atomic layer of the WS₂ at the interface, along with the cationic potential difference. In case of configuration III, the interface has no anionic gradient (due to presence of S in both the layers facing each other) and hence, charge separation is mainly the result of cationic gradient. Therefore, we see different band gaps in configuration III and configuration II. Further, one should always remember, that these configurations are type II and the band edge levels are on two different layers. Therefore, any potential

gradient at interface will definitely effect the corresponding band edge levels. Fig. S1-S6 in SI discuss the electrostatic potential for other vdW HTSs. Fig. S4 explains the change in band gap on the basis of dipole direction. Dipole direction is seen from S to Se i.e. from lower to higher potential. So, we observe opposite dipole directions in configurations II and III, thereby affecting the interfacial interactions. Thus, the vdW HTSs with TMOs are also inline with the above discussion and inference.

Table 2: The Hirshfeld charge and work function of different configurations (I: MoS₂/BX₂, II: MoSSe/BX₂ (Se interfacial layer), III: MoSSe/BX₂ (S interfacial layer))

BX ₂	Hirshfeld charge (e)			Work function (ϕ) (eV)		
	I	II	III	I	II	III
WS ₂	0.64	0.19	3.00	5.19	5.34	4.76
ZrS ₂	-0.26	-0.25	-0.16	5.98	6.02	5.56
HfS ₂	-0.08	-0.14	-0.07	5.98	6.01	5.58
TiS ₂	-0.09	-0.25	-0.12	6.02	6.15	5.69
HfO ₂	-0.04	-0.12	-0.09	6.12	6.13	5.70
T-PtO ₂	0.03	-0.08	-0.04	5.78	5.75	5.53
T-SnO ₂	-0.10	-0.16	-0.06	5.91	5.79	5.46

We have also calculated the associated charge density on the layers and the work function of the vdW HTSs. The work function (ϕ) is significant parameter to understand the charge separation or transfer at the interface. It is defined as follows:

$$\phi = E_{\text{Vac}} - E_{\text{Fermi}}, \quad (2)$$

where E_{Vac} and E_{Fermi} are the electrostatic potential corresponding to the vacuum level and Fermi level, respectively (see Fig. 4). Table 2 gives the total Hirshfeld charge (of all the atoms in the monolayer of the HTS) and the work function of vdW HTSs. The estimated values of the work function of free standing monolayer (ϕ_{M} as in Table 5), have been corroborated with the existing literature^{73*}. The Hirshfeld charge in case of configuration II show greater

*Note that the mentioned reference has considered 15 Å vacuum, which we have found to be converged

charge transfer than that of as in the case of configuration I and III. This is attributed to the anionic and cationic potential difference at the interface. The lesser charge transfer corresponds to the lower work function in configurations I and III. The plane averaged charge density difference $\Delta\rho$ has been calculated (see section V in SI) by:

$$\Delta\rho = \rho(\text{vdW HTSs}) - \rho(\text{MoS}_2 \text{ or MoSSe}) - \rho(\text{BX}_2) \quad (3)$$

where $\rho(\text{vdW HTSs})$, $\rho(\text{MoS}_2)$, $\rho(\text{MoSSe})$ and $\rho(\text{BX}_2)$ are the charge density of the vdW HTS, monolayer MoS_2 , monolayer MoSSe and monolayer BX_2 , respectively.

Table 3: The estimated band bending between vdW HTSs and free-standing monolayer (ϕ_M is the work function of free standing monolayer, I: MoS_2/BX_2 , II: MoSSe/BX_2 (Se interfacial layer), III: MoSSe/BX_2 (S interfacial layer))

BX ₂	ϕ_M (eV)	ΔE_{BB} (eV)		
		I	II	III
WS ₂	5.53	-0.34	-0.19	-0.77
ZrS ₂	6.95	-0.97	-0.93	-1.39
HfS ₂	7.13	-1.15	-1.12	-1.55
TiS ₂	7.01	-0.99	-0.86	-1.32
HfO ₂	8.86	-2.74	-2.73	-3.16
T-PtO ₂	7.86	-2.08	-2.11	-2.33
T-SnO ₂	9.06	-3.15	-3.27	-3.60

We can understand the charge transfer by calculating the band bending (ΔE_{BB}) as well. This parameter is estimated by the Fermi-level difference between the vdW HTSs and the corresponding free-standing monolayer, with the expression as follows:⁷⁶

$$\Delta E_{\text{BB}} = \phi - \phi_M \quad (4)$$

where ϕ is the work function of vdW HTSs and ϕ_M is the work function of free standing at 20 Å vacuum. The slight difference (i.e. not exact match) may be due to this change.

monolayer. The $\Delta E_{\text{BB}} < 0$ indicates charge transfer from the vdW HTSs to the monolayer. All the vdW HTSs, display $\Delta E_{\text{BB}} < 0$ i.e. charge gained by the monolayer (Table 3). The observation is in sync with the calculated Hirshfeld charges as noted in Table 2. It is to be noted that in case of WS_2 , ΔE_{BB} is more negative with $\phi_{\text{M}}(\text{MoS}_2) = 5.82$ eV than that with $\phi_{\text{M}}(\text{WS}_2)$. Hence, the associated Hirshfeld charge on the WS_2 monolayer is positive. The above observations indicate MoSSe based configurations (II and III) to play a crucial role in photocatalytic applications.

The aforementioned discussions along with Fig. 3(a) have showcased the spatial charge separation due to the work function difference. Therefore, with the $e^- - h^+$ pair generation in the individual monolayers of vdW HTSs, the MoS_2 (or MoSSe) monolayer will be positively charged as it contributes to the VBM of vdW HTS, which will restrict the flow of e^- to other layer (BX_2). Moreover, BX_2 monolayer that contributes to the CBm of vdW HTS, does not straddle the reduction potential. Hence, MoS_2 (or MoSSe) monolayer will observe restricted e^- motion from its CBm to BX_2 CBm, thereby facilitating the $e^- - h^+$ recombination path of BX_2 CBm to MoS_2 VBM and promoting the standard Z-scheme mechanism.

Recombination in vdW HTSs

Considering the case of photocatalysts that straddle the potentials, lesser recombination is synchronous with the effective photocatalytic capability. However, vdW HTSs for applicability as Z-scheme photocatalysts, require higher recombination in them as compared to their constituent monolayers. Hence, the layer with CBm above the reduction potential can facilitate HER, while, the layer with VBM below the oxidation potential can facilitate OER. In view of this, we have analyzed the recombination rate, which is indicated by the effective mass of electrons and holes. The effective mass has been calculated by the parabolic fitting at CBm and VBM in the bandstructure obtained by the hybrid calculations.⁷⁷ The bandstructure of $\text{MoS}_2/\text{ZrS}_2$ has been found to be previously reported⁷⁸ and is in sync with that reported in the present work. The similar database of other vdW HTSs discussed here are

previously unreported.

Table 4: The effective mass ratio (D) of the monolayers (BX₂) except MoS₂ and MoSSe (both have same value of D = 1.21)

BX ₂	WS ₂	ZrS ₂	HfS ₂	TiS ₂	HfO ₂	T-PtO ₂	T-SnO ₂
D	1.29	1.58	1.17	0.03	5.88	4.66	9.00

Table 5: The effective mass ratio (D) of the vdW HTSs (I: MoS₂/BX₂, II: MoSSe/BX₂ (Se interfacial layer), III: MoSSe/BX₂ (S interfacial layer))

BX ₂	Effective Mass Ratio (D)		
	I	II	III
WS ₂	2.50	0.85	10.19
ZrS ₂	0.13	0.64	0.62
HfS ₂	0.65	0.87	0.71
TiS ₂	0.50	0.20	0.80
HfO ₂	0.32	0.34	0.34
T-PtO ₂	0.49	0.50	0.49
T-SnO ₂	0.91	1.15	1.14

The recombination in the system can be estimated by relative ratio (D) that is defined as follows:⁷⁹

$$D = m_h^*/m_e^* \tag{5}$$

The higher the variance of D from 1, the lesser is the recombination. Since, D refers to the relative ratio of the effective masses of hole (m_h^*) and electron (m_e^*), its value closer to 1 (i.e low variance) is ideal for high recombination in the system. This is obvious as value closer to 1 indicates similar electron and hole effective masses, resulting in easier recombination. On the contrary, large difference in the effective masses pose significant difference in carrier mobilities leading to the separation of carriers and hindrance in their recombination. Consider, Table 5 that enlists the value of D for monolayers and their corresponding vdW HTSs. The effective

mass of carriers at CBm (i.e. m_e^*) and VBM (i.e. m_h^*) have been obtained along the designated direction in the high symmetry path $\Gamma - M - K - \Gamma$ (see bandstructures i.e. Fig. S7 in SI). Also, it should be noted that the parameter is calculated from the bandstructures of the supercell than the primitive cells. Since, the supercell is small, the density of the bands near the VBM and CBm is not very high and hence, the band folding is not an issue here.

Further, since we are considering Z-scheme photocatalysis, we require monolayer with lesser recombination as compared to that of their corresponding vdW HTSs. In order to review this we have checked the variance of D values from 1 for monolayers and vdW HTSs. Therefore, the vdW HTSs with lesser variance as compared to that of their respective monolayer can be considered probable for Z-scheme photocatalysis. As per the discussed approach, we have deduced MoSSe/ZrS₂ (configuration II and III), MoSSe/HfS₂ (configuration II), MoSSe/TiS₂ (configuration III), MoS₂/SnO₂ and MoSSe/SnO₂ (configuration II and III) as the probable Z-scheme vdW HTSs. Amongst these, the MoS₂/SnO₂, MoSSe/HfS₂ (configuration II) and MoSSe/TiS₂ (configuration III) have shown least variance from 1. Their respective carrier mobilities⁸⁰ are computed as $46 \times 10^2 \text{ cm}^2\text{V}^{-1}\text{s}^{-1}$, $21 \times 10^2 \text{ cm}^2\text{V}^{-1}\text{s}^{-1}$ and $2 \times 10^2 \text{ cm}^2\text{V}^{-1}\text{s}^{-1}$. Additional details are provided in the supplementary material. Note that, we have also estimated their exciton binding energy (E_B), which showed comparatively smaller E_B of vdW HTSs as compared to that of MoS₂ and MoSSe monolayers (see section VII in SI). It should be mentioned here that the value D is an indicative approach and should not be considered as the sole criteria for $e^- - h^+$ recombination. This yields future scope to explore more on carrier dynamics to understand the excitonic physics in these materials. We have, in addition, nevertheless, complied to the inferences with the study of optical response, carrier mobility, H₂O adsorption and HER.

Absorption spectra

Optical response is amongst the important parameters involved in constructing the photocatalytic devices. Therefore, we have obtained the same for previously discussed vdW HTSs,

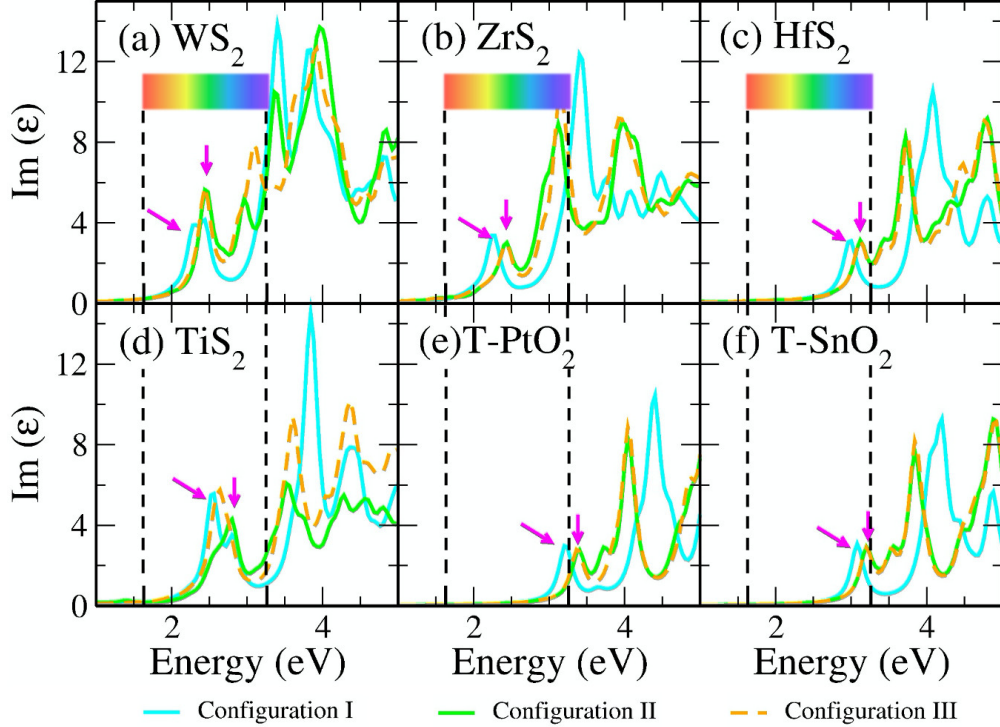


Figure 5: (Color online) Imaginary part of dielectric function vs. energy plot depicting the optical response of the vdW HTS configurations I, II and III by $G_0W_0@HSE06$. Here, the arrow indicates the initial peak position that is associated with the absorption onset.

that can be considered for the photocatalytic applications. Fig. 5 gives the absorption spectra obtained from imaginary part of the dielectric function as computed by GW method ($G_0W_0@HSE06$). The dielectric function is a frequency dependent complex function ($\epsilon(\omega) = \text{Re}(\epsilon) + \text{Im}(\epsilon)$) where the real part ($\text{Re}(\epsilon)$) is computed from the Kramers-Kronig relation and the imaginary part ($\text{Im}(\epsilon)$) is obtained from the interband matrix elements in the momentum space.⁸¹ Since, the interband process consists of transitions to the unoccupied orbitals, the $\text{Im}(\epsilon)$ gives the absorption spectra. The first peak will, therefore, indicate the onset of absorption process. We observe that the vdW HTSs of MoS_2/TMD and MoS_2/TMO have response in the visible region. The spectra corresponding to MoSSe vdW HTSs (configuration II and III) have shown minute blue shift as compared to that of MoS_2 vdW HTSs. Further, we observe from Fig. 5(b) that the vdW HTSs with ZrS_2 and TiS_2 monolayer show red shift as compared to other vdW HTSs (i.e., Fig. 5(a), (c), (d)-(f)). The spectra, thus, indicate the use of $\text{MoS}_2/\text{ZrS}_2$, $\text{MoSSe}/\text{ZrS}_2$, $\text{MoS}_2/\text{TiS}_2$ and $\text{MoSSe}/\text{TiS}_2$ for harnessing

the overlap region of $\text{Im}(\epsilon)$ with the solar spectrum in order to construct the photocatalytic devices.

H₂O Adsorption

Table 6: H₂O adsorption on the monolayer surface

BX ₂	E _{ads} (eV)	Distance (Å)
WS ₂	-0.09	2.88
ZrS ₂	-0.24	2.59
HfS ₂	-0.23	2.75
TiS ₂	-0.25	2.74
T-PtO ₂	-0.28	2.08
T-SnO ₂	-0.29	2.31

We have further calculated the H₂O adsorption in these vdW HTSs to confirm that the adsorption is supported for further redox reactions. The associated expression is as given:

$$E_{\text{ads}} = E(\text{adsorbed H}_2\text{O}) - E(\text{vdW HTSs}) - E(\text{H}_2\text{O}) \tag{6}$$

where, E_{ads} is the adsorption energy (see Table 6) of the H₂O on the vdW HTSs; $E(\text{adsorbed H}_2\text{O})$ is the energy of the vdW HTSs with adsorbed H₂O, $E(\text{vdW HTSs})$ is the energy of the vdW HTSs and $E(\text{H}_2\text{O})$ is the energy of the water molecule. From the Table 6 we observe, H₂O is physisorbed in the system and its binding strength in all the monolayers is higher than that in case of WS₂. Also, the transition metal oxides show higher binding strength than the transition metal dichalcogenides. The data supplement the analysis for considering the monolayers for Z-scheme photocatalysis.

In addition, we have calculated the Gibb's free energy change (ΔG) of the intermediate in

the HER as per the expression:

$$\Delta G = \Delta E + \Delta E_{\text{zpe}} - T\Delta S \quad (7)$$

where ΔE is the intermediate adsorption energy on the vdW HTSs, ΔE_{zpe} is the change in zero-point energy and ΔS is the difference of entropy. The temperature, T , is taken as 300K. We have calculated the E_{zpe} and TS by the following expression using Density Functional Perturbation Theory (DFPT):

$$E_{\text{ZPE}} = \frac{1}{2} \sum_i h\nu_i \quad (8)$$

$$TS = \sum_i h\nu_i \frac{1}{\exp(\frac{h\nu_i}{k_B T}) - 1} - k_B T \sum_i \ln \left[1 - \exp(-\frac{h\nu_i}{k_B T}) \right] \quad (9)$$

where h is Planck's constant, ν_i is vibrational frequencies and k_B is Boltzmann constant. The HER diagram along the reaction pathway $\text{H}^+ + \text{e}^- \rightarrow \text{H}^* \rightarrow 1/2 \text{H}_2$ is illustrated in the Fig. 6. Here, H^* represents the adsorbed intermediate. Under the consideration of $\text{pH} = 0$ and Standard Hydrogen Electrode (SHE) potential of 0 V the $\text{H}^+ + \text{e}^-$ is equivalent to the $1/2 \text{H}_2$.

Now, upon systematically revisiting all the aforementioned factors, we have observed vdW HTSs to be type II with their work function being affected by the interfacial potential difference. This further influences the charge separation. Another point is that the smaller conduction band offset between the two monolayer systems would promote efficient charge separation at the interface.⁸² Therefore, in reference to Fig. 3, with comparatively large difference in two conduction band levels along with type II alignment, the consideration for interlayer recombination in vdW HTSs for Z-scheme process seems very much plausible. Effective mass being the important factor for the same, we have indicated the recombination probability by the effective mass ratio (D). However, since this approach is qualitative we have explicitly included the results of optical response, H_2O adsorption and HER as direct evidences to validate MoSSe/HfS₂, MoSSe/TiS₂, MoS₂/T-SnO₂, MoSSe/T-SnO₂, MoS₂/ZrS₂

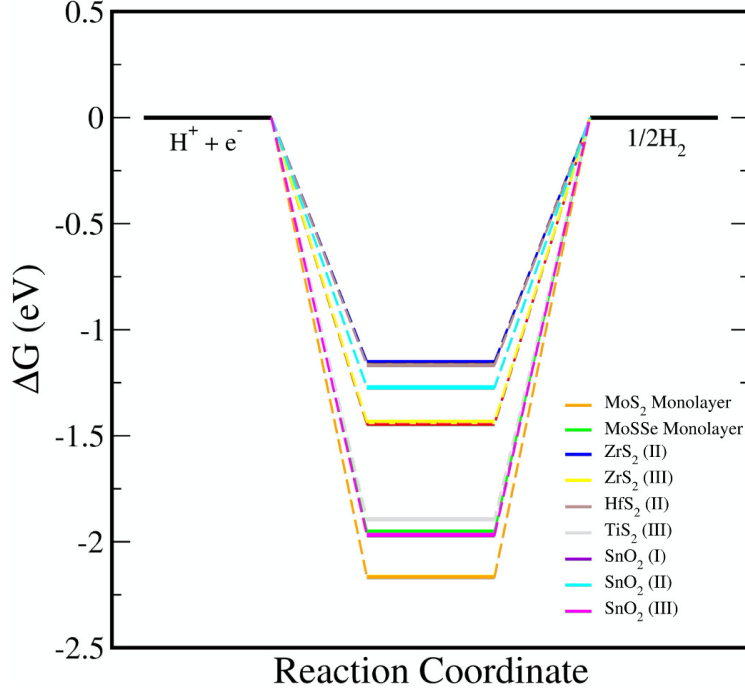


Figure 6: (Color online) The HER reaction free energy diagrams on monolayer and vdW HTSs at an electrode potential $E_{\text{SHE}} = 0$ V and pH = 0. At zero potential, $(\text{H}^+ + \text{e}^-)$ can be expressed as $1/2 \text{H}_2$.

and MoSSe/ZrS₂ are probable Z-scheme photocatalysts.

Conclusion

An exhaustive study has been undertaken for understanding different MoS₂ and MoSSe based vdW HTSs. As per the band edge alignment, it is observed that these vdW HTSs do not facilitate the normal photocatalytic process as they do not straddle the redox potential. However, these are predicted to be implementing the natural photocatalysis by Z-scheme. The band edge alignment of the MoSSe vdW HTSs has inferred large band gap in configuration III than in case of configuration II. This has been attributed to the additional anionic potential gradient due to Se atomic layer at the interface in configuration II. The probability of recombination as implicated by the effective mass ratio (D) has corroborated the MoSSe/HfS₂, MoSSe/TiS₂, MoS₂/T-SnO₂, MoSSe/T-SnO₂, MoS₂/ZrS₂ and MoSSe/ZrS₂ as favourable Z-scheme photocatalyst. The absorption spectra further confirm the visible light

response of these vdW HTSs and hence, their applicability in the photocatalytic devices. Finally, the H₂O adsorption and HER indicate their interaction with water to help in the photocatalytic process.

Supporting Information

(I) Electrostatic Potential. (II) Lattice Parameters. (III) Band Gaps of Configurations. (IV) Bandstructures of Z-scheme vdW HTSs. (V) Planar Averaged Charged Density. (VI) Absorption Spectra of Monolayers. (VII) Exciton Binding Energy (VIII) Carrier Mobility.

Acknowledgement

AS acknowledges IIT Delhi for the financial support. AS and MJ thank Pooja Basera for helpful discussions. MJ acknowledges CSIR, India, for the senior research fellowship [grant no. 09/086(1344)/2018-EMR-I]. SB acknowledges the financial support SERB under his Core Research Grant [CRG/2019/000647]. We acknowledge the High Performance Computing (HPC) facility at IIT Delhi for computational resources.

References

- (1) Ni, M.; Leung, M. K.; Leung, D. Y.; Sumathy, K. A review and recent developments in photocatalytic water-splitting using TiO₂ for hydrogen production. *Renewable and Sustainable Energy Reviews* **2007**, *11*, 401–425.
- (2) Yao, H.; Fan, M.; Wang, Y.; Luo, G.; Fei, W. Magnetic titanium dioxide based nano-materials: synthesis, characteristics, and photocatalytic application in pollutant degradation. *Journal of Materials Chemistry A* **2015**, *3*, 17511–17524.

- (3) Opoku, F.; Govender, K. K.; van Sittert, C. G. C. E.; Govender, P. P. Role of MoS₂ and WS₂ monolayers on photocatalytic hydrogen production and the pollutant degradation of monoclinic BiVO₄: A first-principles study. *New Journal of Chemistry* **2017**, *41*, 11701–11713.
- (4) Yu, C.; Chen, F.; Zeng, D.; Xie, Y.; Zhou, W.; Liu, Z.; Wei, L.; Yang, K.; Li, D. A facile phase transformation strategy for fabrication of novel Z-scheme ternary heterojunctions with efficient photocatalytic properties. *Nanoscale* **2019**, *11*, 7720–7733.
- (5) Gupta, A.; Sakthivel, T.; Seal, S. Recent development in 2D materials beyond graphene. *Progress in Materials Science* **2015**, *73*, 44–126.
- (6) Singh, A.; Basera, P.; Saini, S.; Kumar, M.; Bhattacharya, S. Importance of Many-Body Dispersion in the Stability of Vacancies and Antisites in Free-Standing Monolayer of MoS₂ from First-Principles Approaches. *The Journal of Physical Chemistry C* **2020**, *124*, 1390–1397.
- (7) Chen, Y.; Huang, S.; Ji, X.; Adepalli, K.; Yin, K.; Ling, X.; Wang, X.; Xue, J.; Dresselhaus, M.; Kong, J., et al. Tuning electronic structure of single layer MoS₂ through defect and interface engineering. *ACS nano* **2018**, *12*, 2569–2579.
- (8) Rao, C.; Gopalakrishnan, K.; Maitra, U. Comparative study of potential applications of graphene, MoS₂, and other two-dimensional materials in energy devices, sensors, and related areas. *ACS applied materials & interfaces* **2015**, *7*, 7809–7832.
- (9) Singh, E.; Singh, P.; Kim, K. S.; Yeom, G. Y.; Nalwa, H. S. Flexible molybdenum disulfide (MoS₂) atomic layers for wearable electronics and optoelectronics. *ACS applied materials & interfaces* **2019**, *11*, 11061–11105.
- (10) Zeng, H.; Liu, G.-B.; Dai, J.; Yan, Y.; Zhu, B.; He, R.; Xie, L.; Xu, S.; Chen, X.; Yao, W., et al. Optical signature of symmetry variations and spin-valley coupling in atomically thin tungsten dichalcogenides. *Scientific reports* **2013**, *3*, 1608.

- (11) Wang, C.-Y.; Guo, G.-Y. Nonlinear optical properties of transition-metal dichalcogenide MX₂ (M= Mo, W; X= S, Se) monolayers and trilayers from first-principles calculations. *The Journal of Physical Chemistry C* **2015**, *119*, 13268–13276.
- (12) Glebko, N.; Aleksandrova, I.; Tewari, G. C.; Tripathi, T. S.; Karppinen, M.; Karttunen, A. J. Electronic and vibrational properties of TiS₂, ZrS₂, and HfS₂: Periodic trends studied by dispersion-corrected hybrid density functional methods. *The Journal of Physical Chemistry C* **2018**, *122*, 26835–26844.
- (13) Lau, K. W.; Cocchi, C.; Draxl, C. Electronic and optical excitations of two-dimensional ZrS₂ and HfS₂ and their heterostructure. *Physical Review Materials* **2019**, *3*, 074001.
- (14) Mattinen, M.; Popov, G.; Vehkama ki, M.; King, P. J.; Mizohata, K.; Jalkanen, P.; Ra isa nen, J.; Leskela , M.; Ritala, M. Atomic layer deposition of emerging 2D semi-conductors, HfS₂ and ZrS₂, for optoelectronics. *Chemistry of Materials* **2019**, *31*, 5713–5724.
- (15) Lebègue, S.; Björkman, T.; Klintenberg, M.; Nieminen, R. M.; Eriksson, O. Two-dimensional materials from data filtering and ab initio calculations. *Physical Review X* **2013**, *3*, 031002.
- (16) Yang, J.; Zeng, Z.; Kang, J.; Betzler, S.; Czarnik, C.; Zhang, X.; Ophus, C.; Yu, C.; Bustillo, K.; Pan, M., et al. Formation of two-dimensional transition metal oxide nanosheets with nanoparticles as intermediates. *Nature materials* **2019**, *18*, 970–976.
- (17) Leong, C. C.; Pan, H.; Ho, S. K. Two-dimensional transition-metal oxide monolayers as cathode materials for Li and Na ion batteries. *Physical Chemistry Chemical Physics* **2016**, *18*, 7527–7534.
- (18) Liao, P.; Carter, E. A. New concepts and modeling strategies to design and evaluate photo-electro-catalysts based on transition metal oxides. *Chemical Society Reviews* **2013**, *42*, 2401–2422.

- (19) Ju, L.; Bie, M.; Shang, J.; Tang, X.; Kou, L. Janus transition metal dichalcogenides: A superior platform for photocatalytic water splitting. *Journal of Physics: Materials* **2020**, *3*, 022004.
- (20) Sun, Y.; Shuai, Z.; Wang, D. Janus monolayer of WSeTe, a new structural phase transition material driven by electrostatic gating. *Nanoscale* **2018**, *10*, 21629–21633.
- (21) Song, B.; Liu, L.; Yam, C. Suppressed Carrier Recombination in Janus MoSSe Bilayer Stacks: A Time-Domain Ab Initio Study. *The journal of physical chemistry letters* **2019**, *10*, 5564–5570.
- (22) Sun, M.; Schwingenschlogl, U. B2P6: A Two-dimensional anisotropic Janus material with potential in photocatalytic water splitting and metal-ion batteries. *Chemistry of Materials* **2020**, *32*, 4795–4800.
- (23) Ma, X.; Wu, X.; Wang, H.; Wang, Y. A Janus MoSSe monolayer: a potential wide solar-spectrum water-splitting photocatalyst with a low carrier recombination rate. *Journal of Materials Chemistry A* **2018**, *6*, 2295–2301.
- (24) Luo, Y.; Wang, S.; Shu, H.; Chou, J.-P.; Ren, K.; Yu, J.; Sun, M. A MoSSe/blue phosphorene vdw heterostructure with energy conversion efficiency of 19.9% for photocatalytic water splitting. *Semiconductor Science and Technology* **2020**, *35*, 125008.
- (25) Kuc, A.; Heine, T. The electronic structure calculations of two-dimensional transition-metal dichalcogenides in the presence of external electric and magnetic fields. *Chemical Society Reviews* **2015**, *44*, 2603–2614.
- (26) Kumar, R.; Verzhbitskiy, I.; Giustiniano, F.; Sidiropoulos, T. P.; Oulton, R. F.; Eda, G. Interlayer screening effects in WS₂/WSe₂ van der Waals hetero-bilayer. *2D Materials* **2018**, *5*, 041003.

- (27) Huang, Y.; Chen, X.; Wang, C.; Peng, L.; Qian, Q.; Wang, S. Layer-dependent electronic properties of phosphorene-like materials and phosphorene-based van der Waals heterostructures. *Nanoscale* **2017**, *9*, 8616–8622.
- (28) Terrones, H.; López-Urías, F.; Terrones, M. Novel hetero-layered materials with tunable direct band gaps by sandwiching different metal disulfides and diselenides. *Scientific reports* **2013**, *3*, 1–7.
- (29) Zhang, Q.; Schwingenschlögl, U. Rashba effect and enriched spin-valley coupling in Ga X/M X₂ (M= Mo, W; X= S, Se, Te) heterostructures. *Physical Review B* **2018**, *97*, 155415.
- (30) Rivera, P.; Seyler, K. L.; Yu, H.; Schaibley, J. R.; Yan, J.; Mandrus, D. G.; Yao, W.; Xu, X. Valley-polarized exciton dynamics in a 2D semiconductor heterostructure. *Science* **2016**, *351*, 688–691.
- (31) Li, P.; Zhang, W.; Li, D.; Liang, C.; Zeng, X. C. Multifunctional Binary Monolayers Ge_xP_y: Tunable Band Gap, Ferromagnetism, and Photocatalyst for Water Splitting. *ACS applied materials & interfaces* **2018**, *10*, 19897–19905.
- (32) Li, P.; Zhang, W.; Liang, C.; Zeng, X. C. Two-dimensional MgX₂Se₄ (X= Al, Ga) monolayers with tunable electronic properties for optoelectronic and photocatalytic applications. *Nanoscale* **2019**, *11*, 19806–19813.
- (33) Luo, Y.; Ren, K.; Wang, S.; Chou, J.-P.; Yu, J.; Sun, Z.; Sun, M. First-principles study on transition-metal dichalcogenide/BSe van der Waals heterostructures: A promising water-splitting photocatalyst. *The Journal of Physical Chemistry C* **2019**, *123*, 22742–22751.
- (34) Luo, Y.; Wang, S.; Ren, K.; Chou, J.-P.; Yu, J.; Sun, Z.; Sun, M. Transition-metal dichalcogenides/Mg(OH)₂ van der Waals heterostructures as promising water-splitting

- photocatalysts: a first-principles study. *Physical Chemistry Chemical Physics* **2019**, *21*, 1791–1796.
- (35) Ren, K.; Wang, S.; Luo, Y.; Chou, J.-P.; Yu, J.; Tang, W.; Sun, M. High-efficiency photocatalyst for water splitting: a Janus MoSSe/XN (X= Ga, Al) van der Waals heterostructure. *Journal of Physics D: Applied Physics* **2020**, *53*, 185504.
- (36) Wang, S.; Ren, C.; Tian, H.; Yu, J.; Sun, M. MoS₂/ZnO van der Waals heterostructure as a high-efficiency water splitting photocatalyst: a first-principles study. *Physical Chemistry Chemical Physics* **2018**, *20*, 13394–13399.
- (37) Li, Y.; Li, Y.-L.; Araujo, C. M.; Luo, W.; Ahuja, R. Single-layer MoS₂ as an efficient photocatalyst. *Catalysis Science & Technology* **2013**, *3*, 2214–2220.
- (38) Parzinger, E.; Miller, B.; Blaschke, B.; Garrido, J. A.; Ager, J. W.; Holleitner, A.; Wurstbauer, U. Photocatalytic stability of single-and few-layer MoS₂. *ACS nano* **2015**, *9*, 11302–11309.
- (39) Tang, Z.-K.; Yin, W.-J.; Zhang, L.; Wen, B.; Zhang, D.-Y.; Liu, L.-M.; Lau, W.-M. Spatial separation of photo-generated electron-hole pairs in BiOBr/BiOI bilayer to facilitate water splitting. *Scientific reports* **2016**, *6*, 32764.
- (40) Gao, X.; Shen, Y.; Ma, Y.; Wu, S.; Zhou, Z. A water splitting photocatalysis: blue phosphorus/g-GeC van der Waals heterostructure. *Applied Physics Letters* **2019**, *114*, 093902.
- (41) Zhang, R.; Zhang, L.; Zheng, Q.; Gao, P.; Zhao, J.; Yang, J. Direct Z-scheme water splitting photocatalyst based on two-dimensional Van Der Waals heterostructures. *The journal of physical chemistry letters* **2018**, *9*, 5419–5424.
- (42) Ren, K.; Ren, C.; Luo, Y.; Xu, Y.; Yu, J.; Tang, W.; Sun, M. Using van der Waals heterostructures based on two-dimensional blue phosphorus and XC (X= Ge, Si) for

- water-splitting photocatalysis: a first-principles study. *Physical Chemistry Chemical Physics* **2019**, *21*, 9949–9956.
- (43) Wang, B.-J.; Li, X.-H.; Zhao, R.; Cai, X.-L.; Yu, W.-Y.; Li, W.-B.; Liu, Z.-S.; Zhang, L.-W.; Ke, S.-H. Electronic structures and enhanced photocatalytic properties of blue phosphorene/BSe van der Waals heterostructures. *Journal of Materials Chemistry A* **2018**, *6*, 8923–8929.
- (44) Fu, C.-F.; Luo, Q.; Li, X.; Yang, J. Two-dimensional van der Waals nanocomposites as Z-scheme type photocatalysts for hydrogen production from overall water splitting. *Journal of Materials Chemistry A* **2016**, *4*, 18892–18898.
- (45) Liu, Y.; Zeng, X.; Easton, C. D.; Li, Q.; Xia, Y.; Yin, Y.; Hu, X.; Hu, J.; Xia, D.; McCarthy, D. T., et al. An in situ assembled WO₃-TiO₂ vertical heterojunction for enhanced Z-scheme photocatalytic activity. *Nanoscale* **2020**, *12*, 8775–8784.
- (46) Xia, X.; Song, M.; Wang, H.; Zhang, X.; Sui, N.; Zhang, Q.; Colvin, V. L.; William, W. Y. Latest progress in constructing solid-state Z scheme photocatalysts for water splitting. *Nanoscale* **2019**, *11*, 11071–11082.
- (47) Maeda, K. Z-scheme water splitting using two different semiconductor photocatalysts. *ACS Catalysis* **2013**, *3*, 1486–1503.
- (48) Li, H.; Tu, W.; Zhou, Y.; Zou, Z. Z-Scheme photocatalytic systems for promoting photocatalytic performance: recent progress and future challenges. *Advanced Science* **2016**, *3*, 1500389.
- (49) Bard, A. J. Photoelectrochemistry and heterogeneous photocatalysis at semiconductors. *Journal of Photochemistry* **1979**, *10*, 59–75.
- (50) Lang, J.; Hu, Y. H. Phosphorus-based metal-free Z-scheme 2D van der Waals het-

- erostructures for visible-light photocatalytic water splitting: a first-principles study. *Physical Chemistry Chemical Physics* **2020**, *22*, 9250–9256.
- (51) Ju, L.; Dai, Y.; Wei, W.; Li, M.; Huang, B. DFT investigation on two-dimensional GeS/WS₂ van der Waals heterostructure for direct Z-scheme photocatalytic overall water splitting. *Applied Surface Science* **2018**, *434*, 365–374.
- (52) Rasmussen, F. A.; Thygesen, K. S. Computational 2D materials database: electronic structure of transition-metal dichalcogenides and oxides. *The Journal of Physical Chemistry C* **2015**, *119*, 13169–13183.
- (53) Martin, R. M. *Electronic structure: basic theory and practical methods*; Cambridge university press, 2004.
- (54) Martin, R. M.; Reining, L.; Ceperley, D. M. *Interacting Electrons*; Cambridge University Press, 2016.
- (55) Freysoldt, C.; Grabowski, B.; Hickel, T.; Neugebauer, J.; Kresse, G.; Janotti, A.; Van de Walle, C. G. First-principles calculations for point defects in solids. *Reviews of modern physics* **2014**, *86*, 253.
- (56) Feng, L.-p.; Su, J.; Chen, S.; Liu, Z.-t. First-principles investigations on vacancy formation and electronic structures of monolayer MoS₂. *Materials Chemistry and Physics* **2014**, *148*, 5–9.
- (57) Hohenberg, P.; Kohn, W. Inhomogeneous electron gas. *Physical review* **1964**, *136*, B864.
- (58) Kohn, W.; Sham, L. J. Self-consistent equations including exchange and correlation effects. *Physical review* **1965**, *140*, A1133.
- (59) Kresse, G.; Furthmüller, J. Efficient iterative schemes for ab initio total-energy calculations using a plane-wave basis set. *Physical review B* **1996**, *54*, 11169.

- (60) Blöchl, P. E. Projector augmented-wave method. *Physical review B* **1994**, *50*, 17953.
- (61) Blum, V.; Gehrke, R.; Hanke, F.; Havu, P.; Havu, V.; Ren, X.; Reuter, K.; Scheffler, M. Ab initio molecular simulations with numeric atom-centered orbitals. *Computer Physics Communications* **2009**, *180*, 2175–2196.
- (62) Stampfl, C.; Van de Walle, C. Density-functional calculations for III-V nitrides using the local-density approximation and the generalized gradient approximation. *Physical Review B* **1999**, *59*, 5521.
- (63) Perdew, J. P.; Burke, K.; Ernzerhof, M. Generalized gradient approximation made simple. *Physical review letters* **1996**, *77*, 3865.
- (64) Heyd, J.; Scuseria, G. E.; Ernzerhof, M. Hybrid functionals based on a screened Coulomb potential. *The Journal of chemical physics* **2003**, *118*, 8207–8215.
- (65) Tkatchenko, A.; Scheffler, M. Accurate molecular van der Waals interactions from ground-state electron density and free-atom reference data. *Physical review letters* **2009**, *102*, 073005.
- (66) Tkatchenko, A.; DiStasio Jr, R. A.; Car, R.; Scheffler, M. Accurate and efficient method for many-body van der Waals interactions. *Physical review letters* **2012**, *108*, 236402.
- (67) Weng, J.; Gao, S.-P. A honeycomb-like monolayer of HfO₂ and the calculation of static dielectric constant eliminating the effect of vacuum spacing. *Physical Chemistry Chemical Physics* **2018**, *20*, 26453–26462.
- (68) Ren, K.; Tang, W.; Sun, M.; Cai, Y.; Cheng, Y.; Zhang, G. A direct Z-scheme PtS₂/arsenene van der Waals heterostructure with high photocatalytic water splitting efficiency. *Nanoscale* **2020**, *12*, 17281–17289.
- (69) Onida, G.; Reining, L.; Rubio, A. Electronic excitations: density-functional versus many-body Green’s-function approaches. *Reviews of modern physics* **2002**, *74*, 601.

- (70) Jiang, H.; Rinke, P.; Scheffler, M. Electronic properties of lanthanide oxides from the G W perspective. *Physical Review B* **2012**, *86*, 125115.
- (71) Rahman, A. U.; Morbec, J. M.; Rahman, G.; Kratzer, P. Commensurate versus incommensurate heterostructures of group-III monochalcogenides. *Physical Review Materials* **2018**, *2*, 094002.
- (72) Bastos, C. M.; Besse, R.; Da Silva, J. L.; Sipahi, G. M. Ab initio investigation of structural stability and exfoliation energies in transition metal dichalcogenides based on Ti-, V-, and Mo-group elements. *Physical Review Materials* **2019**, *3*, 044002.
- (73) Hastrup, S.; Strange, M.; Pandey, M.; Deilmann, T.; Schmidt, P. S.; Hinsche, N. F.; Gjerding, M. N.; Torelli, D.; Larsen, P. M.; Riis-Jensen, A. C., et al. The Computational 2D Materials Database: high-throughput modeling and discovery of atomically thin crystals. *2D Materials* **2018**, *5*, 042002.
- (74) Xia, C.; Xiong, W.; Xiao, W.; Du, J.; Fang, L.; Li, J.; Jia, Y. Enhanced carrier concentration and electronic transport by inserting graphene into van der Waals heterostructures of transition-metal dichalcogenides. *Physical Review Applied* **2018**, *10*, 024028.
- (75) Hu, X.; Kou, L.; Sun, L. Stacking orders induced direct band gap in bilayer MoSe₂-WSe₂ lateral heterostructures. *Scientific reports* **2016**, *6*, 31122.
- (76) Padilha, J.; Fazzio, A.; da Silva, A. J. van der Waals heterostructure of phosphorene and graphene: tuning the Schottky barrier and doping by electrostatic gating. *Physical review letters* **2015**, *114*, 066803.
- (77) Ganose, A.; Jackson, A.; Scanlon, D. sumo: Command-line tools for plotting and analysis of periodic* ab initio* calculations. *Journal of Open Source Software* **2018**, *3*, 717.

- (78) Lu, A. K. A.; Houssa, M.; Luisier, M.; Pourtois, G. Impact of Layer Alignment on the Behavior of MoS₂-ZrS₂ Tunnel Field-Effect Transistors: An Ab Initio Study. *Physical Review Applied* **2017**, *8*, 034017.
- (79) Zhang, H.; Liu, L.; Zhou, Z. First-principles studies on facet-dependent photocatalytic properties of bismuth oxyhalides (BiOXs). *RSC advances* **2012**, *2*, 9224–9229.
- (80) Dai, J.; Zeng, X. C. Titanium trisulfide monolayer: theoretical prediction of a new direct-gap semiconductor with high and anisotropic carrier mobility. *Angewandte Chemie* **2015**, *127*, 7682–7686.
- (81) Basera, P.; Saini, S.; Bhattacharya, S. Self energy and excitonic effect in (un) doped TiO₂ anatase: a comparative study of hybrid DFT, GW and BSE to explore optical properties. *Journal of Materials Chemistry C* **2019**, *7*, 14284–14293.
- (82) Khanchandani, S.; Srivastava, P. K.; Kumar, S.; Ghosh, S.; Ganguli, A. K. Band gap engineering of ZnO using core/shell morphology with environmentally benign Ag₂S sensitizer for efficient light harvesting and enhanced visible-light photocatalysis. *Inorganic Chemistry* **2014**, *53*, 8902–8912.

MoS₂ and Janus (MoSSe) Based 2D van der Waals heterostructures: Emerging Direct Z-scheme Photocatalysts

Arunima Singh*, Manjari Jain, Saswata Bhattacharya*

Department of Physics, Indian Institute of Technology Delhi, New Delhi 110016, India

E-mail: saswata@physics.iitd.ac.in[SB], Arunima.Singh@physics.iitd.ac.in[AS]

Phone: +91-2659 1359. Fax: +91-2658 2037

Supporting Information

- I. Electrostatic Potential
- II. Lattice Parameters
- III. Band Gaps of Configurations
- IV. Bandstructures of Z-scheme vdW HTSs
- V. Planar Averaged Charged Density
- VI. Absorption Spectra of Monolayers
- VII. Exciton Binding Energy
- VIII. Carrier Mobility

I. Electrostatic Potential

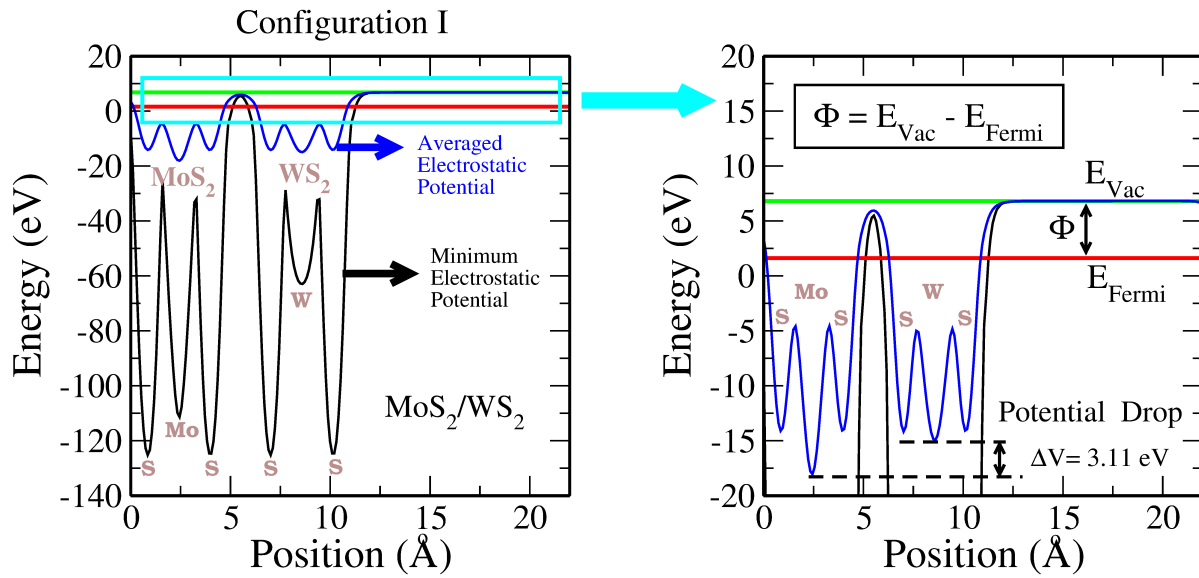


Figure S1: Schematic of electrostatic potential as obtained corresponding to MoS₂/WS₂ vdW HTS.

Averaged Electrostatic Potential

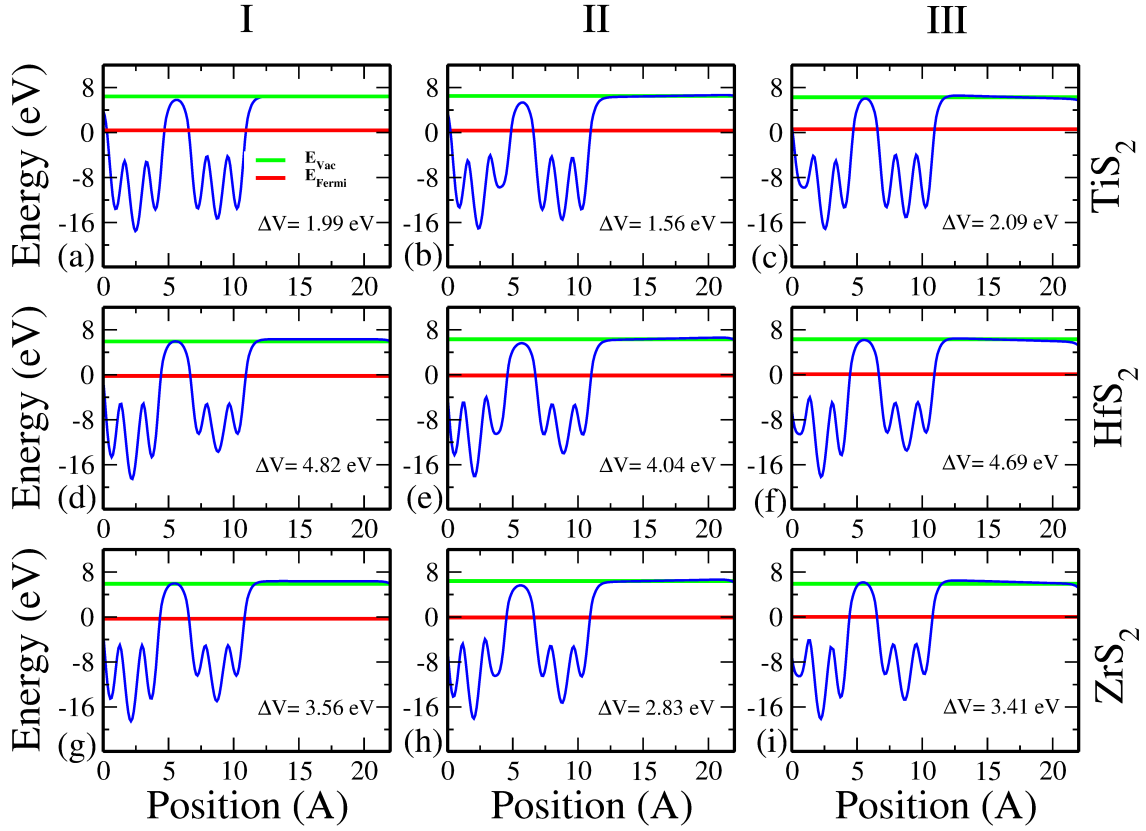


Figure S2: Averaged electrostatic potential corresponding to TMDs viz. TiS_2 (upper panel), HfS_2 (middle panel) and ZrS_2 (lower panel) for I, II and III configurations.

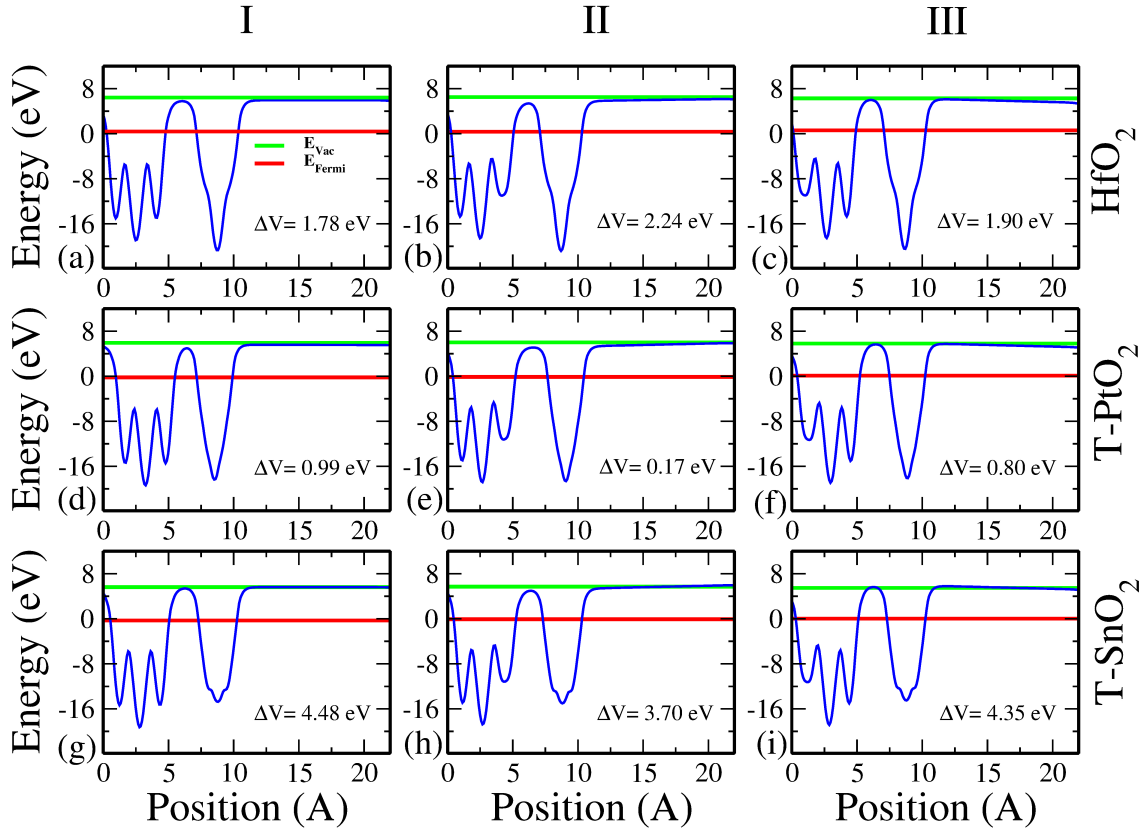


Figure S3: Averaged electrostatic potential corresponding to TMOs viz. HfO_2 (upper panel), T-SnO_2 (middle panel) and T-PtO_2 (lower panel) for I, II and III configurations.

Minimum Electrostatic Potential

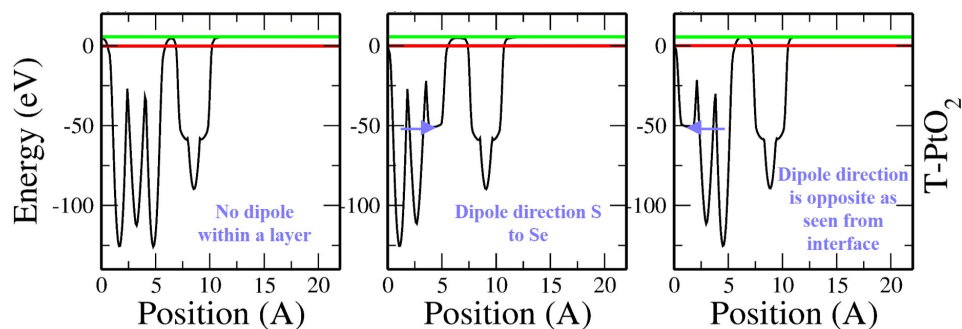


Figure S4: Electrostatic potential of T-PtO₂ for I, II and III configurations, showing dipole direction at the interface.

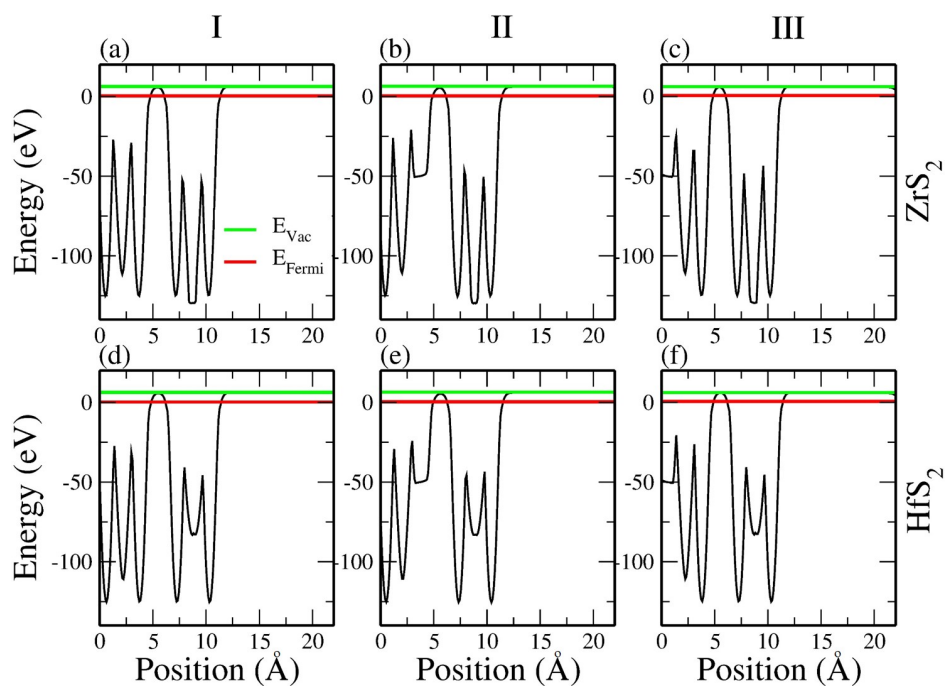


Figure S5: Electrostatic potential corresponding to ZrS₂ (upper panel) and HfS₂ (lower panel) for I, II and III configurations.

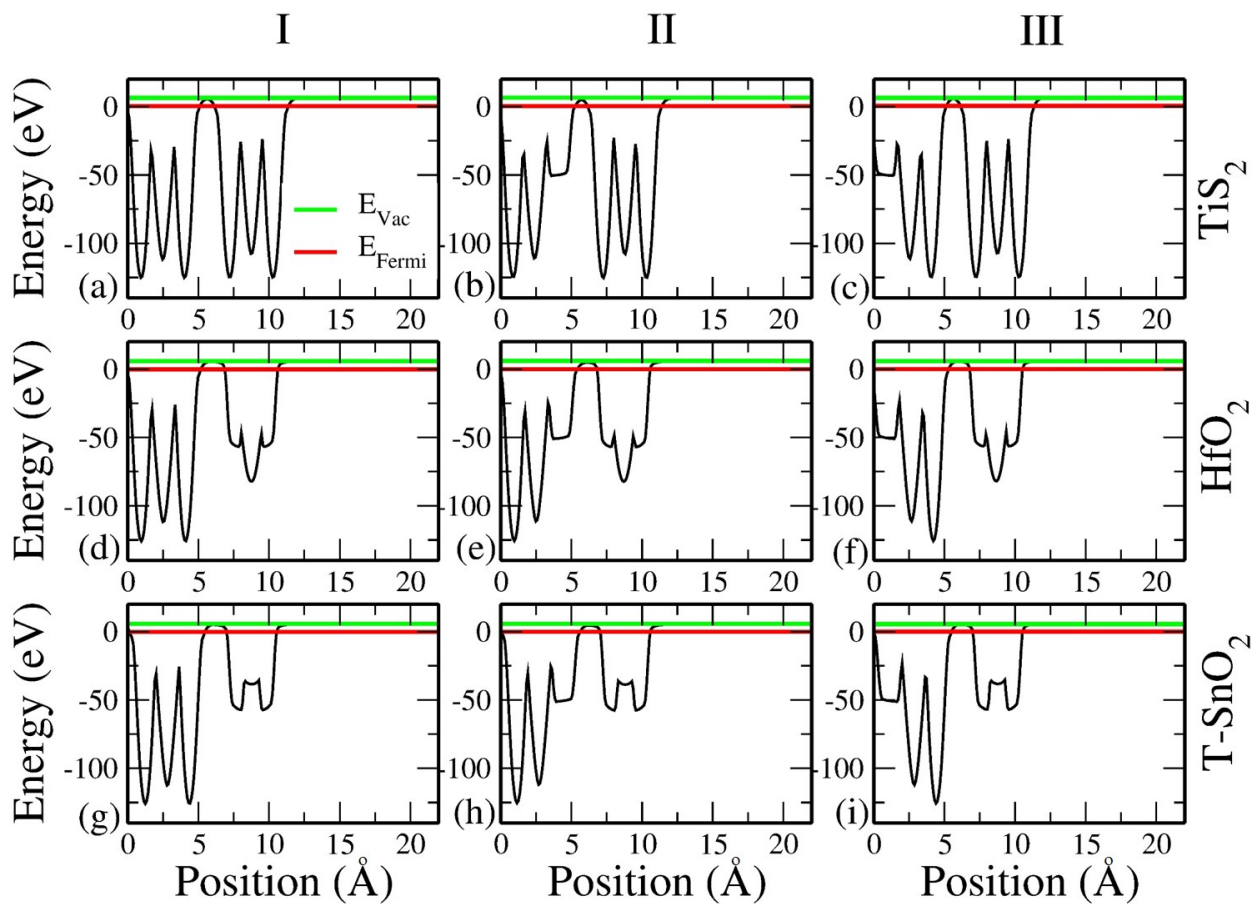


Figure S6: Electrostatic potential corresponding to TiS_2 (upper panel), HfO_2 (middle panel) and SnO_2 (lower panel) for I, II and III configurations.

II. Lattice Parameters

Table S1: Lattice constants (l) of 2×2 monolayers

BX ₂	MoS ₂	WS ₂	ZrS ₂	HfS ₂	TiS ₂	HfO ₂	T-PtO ₂	T-SnO ₂
l	6.321	6.321	7.120	7.019	6.660	6.243	6.296	6.450

III. Band Gaps of Configurations

Table S2: Band gaps of the monolayers and their corresponding vdW HTSs.

BX ₂	Band Gap (eV) (Indirect/Direct)			
	Monolayer	I	II	III
MoS ₂	-/2.257	-	-	-
MoSSe	-/2.172	-	-	-
WS ₂	-/2.447	1.636/2.038	1.879/1.885	1.589/1.928
ZrS ₂	1.829/1.892	0.752/0.809	0.123/0.177	0.676/0.729
HfS ₂	1.937/2.019	0.746/0.863	0.079/0.185	0.663/0.773
TiS ₂	1.672/1.769	0.414/0.418	0.047/0.056	0.520/0.525
HfO ₂	3.516/3.520	0.486/0.499	0.072/0.090	0.440/0.453
T-PtO ₂	3.304/3.313	1.323/1.525	0.595/0.846	1.178/1.423
T-SnO ₂	4.143/4.297	1.130/1.285	0.460/0.882	1.069/1.473

IV. Bandstructures of Z-scheme vdW HTSs

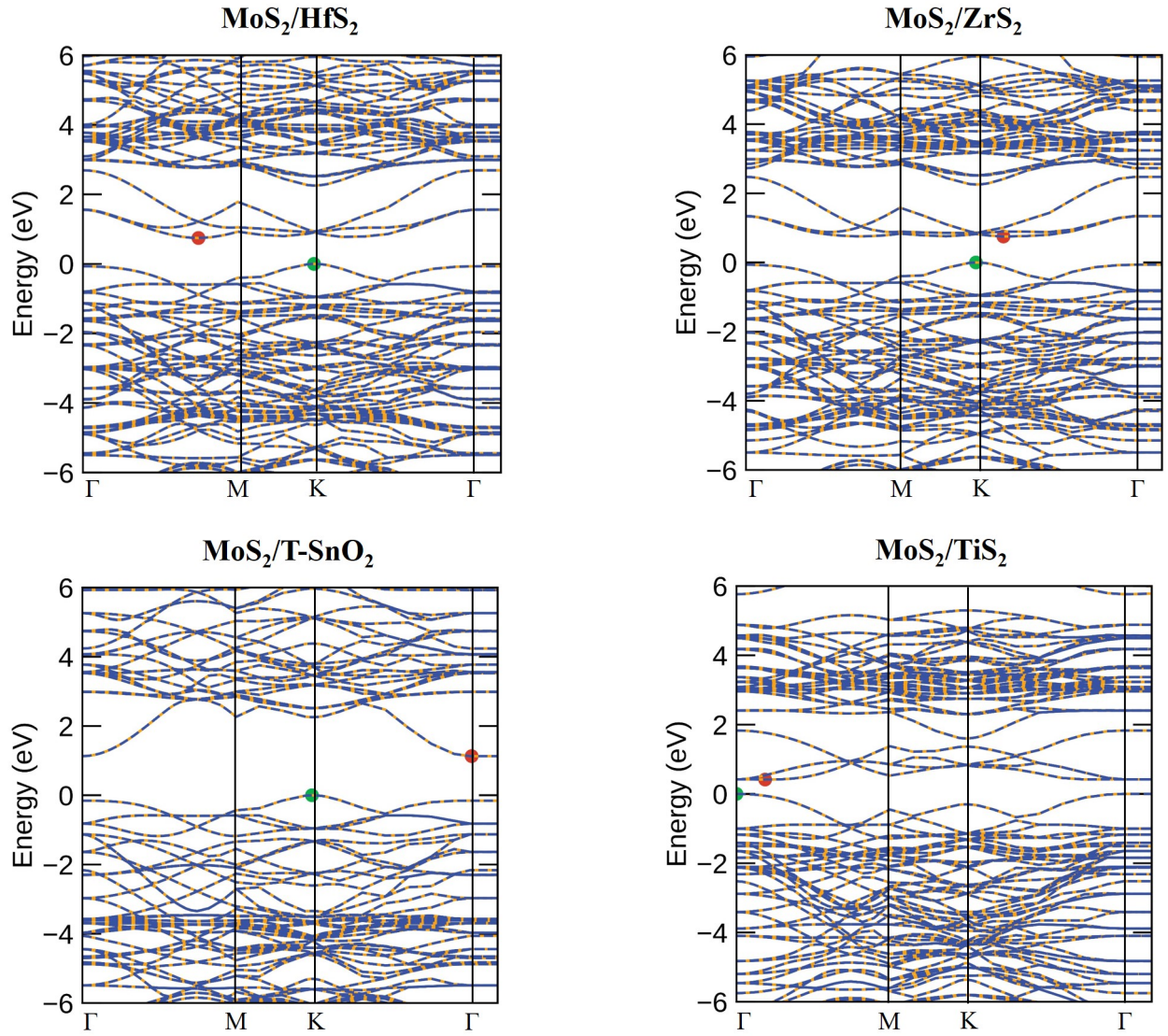


Figure S7: (Color online) Bandstructures corresponding to the supercell of MoS₂/BX₂ HTSs (configuration I) where MoS₂/ZrS₂ has similar bandstructure as that of MoS₂/HfS₂. The bandstructures corresponding to the MoS₂ based vdW HTSs (configurations II and III) are similar with slight change in energetics. The red and green points correspond to the conduction band minimum and valence band maximum.

V. Planar Averaged Charged Density

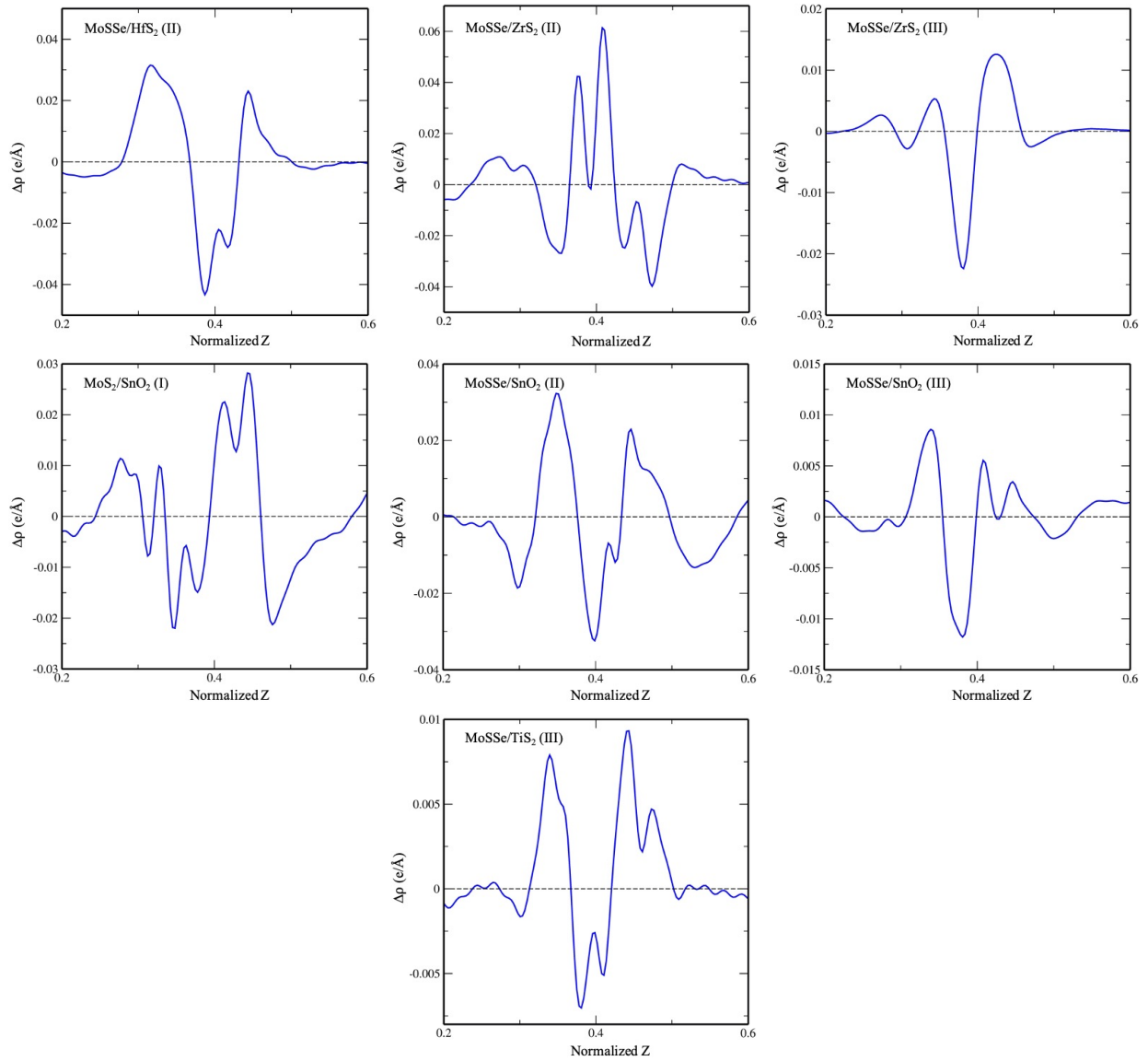


Figure S8: (Color online) Planar averaged charge density

VI. Absorption Spectra of Monolayers

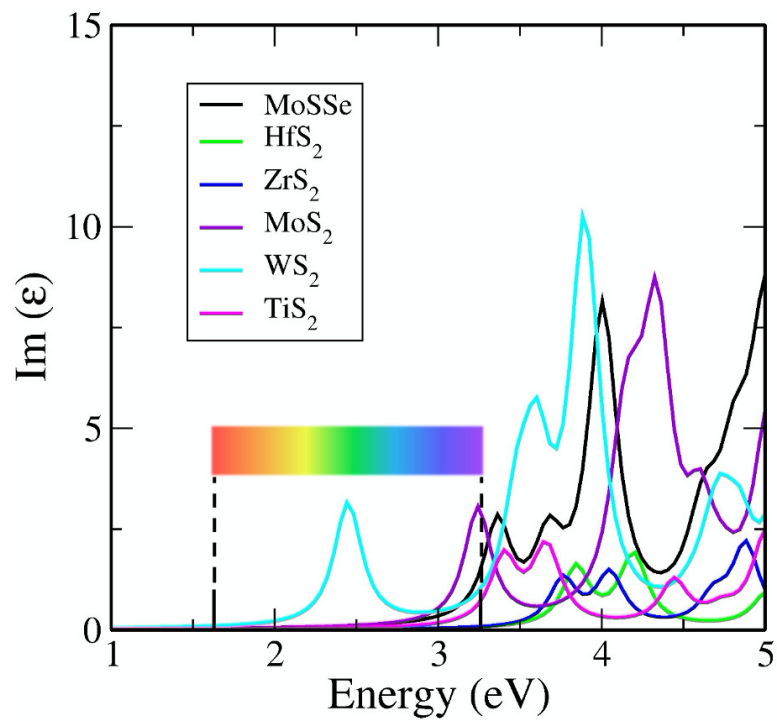


Figure S9: Absorption spectra of Janus (MoSSe) and monolayer TMDs i.e MoS₂, WS₂, TiS₂, HfS₂ and ZrS₂

VII. Exciton Binding Energy

We have performed mBSE calculations, with an intention to simply compare the exciton binding energy (E_B) of vdW HTSs with MoS₂ and MoSSe. We have included four valence and conduction bands for mBSE on top of hybrid functional. However, there is a huge scope in understanding the excitonic transitions in these systems with different computational approaches. Presently, considering the Z-scheme application, the smaller E_B of vdW HTSs as compared to MoS₂ (or MoSSe) would allow more $e^- - h^+$ recombination in vdW HTS thereby facilitating MoS₂ (or MoSSe) for HER.

Table S3: Exciton binding energies of vdW HTSs, MoS₂ and MoSSe monolayers

	MoS ₂	MoSSe	MoSSe/HfS ₂ (II)	MoSSe/TiS ₂ (III)	MoS ₂ /SnO ₂ (I)	MoSSe/ZrS ₂ (II)	MoSSe/ZrS ₂ (III)	MoSSe/SnO ₂ (III)
E_B (eV)	1.5	1.8	0.44	0.37	1.3	0.42	0.41	1.3

VIII. Carrier Mobility

$$\mu = \frac{2e\hbar^3 C}{3k_B T |m^*|^2 E_1^2} \quad (1)$$

In this expression C is defined as $C = [\partial^2 E / \partial \delta^2] / S^0$. E refers to the total energy of the system, δ is the applied uniaxial strain, and S^0 is the area of the optimized vdW HTS. m^* is the effective mass, expressed as $m^* = \hbar^2 (\partial^2 E / \partial k^2)^{-1}$. T represents temperature, and E_1 is the deformation potential constant that is defined as $\Delta E = E_1 (\Delta l / l_0)$. Here, ΔE is the energy shift of the band edge position with respect to the lattice strain $\Delta l / l_0$. The energies of the band edges (CBm or VBM) are obtained with vacuum level as the reference.